An interneuron circuit reproducing essential spectral features of field potentials

Reinoud Maex

reinoud.maex@ens.fr

Ecole Normale Supérieure

rue d'Ulm 29 - Paris 75005 - France

December 10, 2017

Abstract

Recent advances in engineering and signal processing have renewed the interest in invasive and surface brain recordings, yet many features of cortical field potentials remain incompletely understood.

In the present computational study, we show that a model circuit of interneurons, coupled via both $GABA_A$ receptor synapses and electrical synapses, reproduces many essential features of the power spectrum of local field potential (LFP) recordings, such as $1/f$ power scaling at low ($<$ 15 Hz) frequencies, power accumulation in the γ-frequency band (30–100 Hz), and a robust α rhythm in the absence of stimulation. The low-frequency $1/f$ power scaling depends on strong reciprocal inhibition, whereas the α rhythm is generated by electrical coupling of intrinsically active neurons. As in previous studies, the γ power arises through the amplification of single-neuron spectral properties, owing to the refractory period, by parameters that favour neuronal synchrony, such as delayed inhibition. The present study also confirms that both synaptic and voltage-gated membrane currents substantially contribute to the LFP, and that high-frequency signals such as action potentials quickly taper off with distance. Given the ubiquity of electrically coupled interneuron circuits in the mammalian brain, they may be major determinants of the recorded potentials.

Key words: local field potentials, EEG, MEG, power spectrum, $1/f$ scaling, α rhythm, γ power

1 Introduction

Local-circuit currents around pools of neurons generate an electric field in the resistive medium that constitutes extracellular space. The associated potentials can be recorded either invasively as local field potentials (LFPs) (Lorente de No, 1947), or with surface electrodes as in EEG and MEG. The currents are mainly driven by voltage- and ligand-gated membrane channels, and hence the measured potential is often used to infer neuronal activity or connectivity patterns (Rall & Shepherd, 1968; Einevoll et al., 2013).

The most frequently used method of LFP analysis is to calculate its power spectrum, and compare different frequency bands that have been associated with different behavioural states (Buzsáki, 2006). Well-established features of the power spectrum of awake scalp or LFP recordings are an approximate $1/f$ scaling at low frequencies, a concentration of power in the γ band (30–100 Hz) during active processing, and strong rhythmic activity in the α band (8–12 Hz) in the absence of sensory stimulation (Nunez, 1981; Novikov et al., 1997; Bédard et al., 2006; Fries et al., 2008).

The role of inhibitory interneurons in the generation of γ activity has been convincingly demonstrated (Wang & Buzsáki, 1996; Buzsáki & Wang, 2012). We here present an interneuron circuit model that generates not only γ activity but also an α rhythm and $1/f$ scaling.

2 The interneuron circuit model

The model is a biophysically detailed implementation of the circuit of inhibitory interneurons (stellate and basket cells) of the molecular layer of the cerebellar cortex (for a more complete description of both the actual circuit and the model, see Maex & Gutkin (2017) and references therein). The advantage of modelling cerebellar cortex is its almost crystal-like organization, with most axons following a one-dimensional course in either the sagittal (inhibitory interneurons) or transverse (excitatory parallel fibers) direction (Fig. 1A).

2.1 Model description

In brief, the circuit comprised a strip of the molecular layer of cerebellar cortex, 720 μm along the sagittal direction, 100 μm wide (the width of a microzone) and 220 μm deep (almost the

entire depth of the molecular layer of cerebellar cortex) (Fig. 1, B and C). It contained 800 (40 x 5 x 4) interneurons that were identical but for a randomization of their leak potential.

The 22-compartmental interneuron model had an active soma and three isoplanar passive dendrites of seven compartments each, as in Abrahamsson et al. (2012). The active soma channels were: a fast spike-generating inactivating Na channel (InNa); T-type (CaT) and L-type (CaHVA) Ca channels; delayed-rectifier (KDr) and inactivating (KA) K channels; a both voltage- and Ca-activated BK-channel (KC); and an hyperpolarization-activated h current (h). The neurons did not burst, nor did they exhibit spike-rate adaptation.

Dendritic excitation was provided via AMPA receptor (AMPAR) synapses by a pool of 8860 parallel fibres (PFs), which made 3 ± 1.9 synapses on average (± standard deviation). Conversely, an interneuron received 33.2 ± 5.8 PF synapses. Only pairs of interneurons aligned on the same PF axis shared considerable PF input (average 20 %). Changing the amount of correlated AMPAR input did not change the results. The model did not contain NMDA receptor synapses, which on actual interneurons are located extra-synaptically.

Typical interneurons have a bipolar architecture with their dendrite and axon running in opposite directions. Half the model interneurons had their axon running rostrally, half caudally (Fig. 1B). Each axon formed two ellipsoid plexi of $GABA_A$ receptor ($GABA_AR$) synapses: a proximal one centred 40 μm from the soma and primarily implementing self-inhibition ('self' referring to the sub-populations of interneurons partly receiving shared excitation) and a distal one at 160 μm implementing lateral inhibition. In the present version of the model, most synapses between the interneurons were laid by the distal kernel, which enhanced the circuit integration time (Maex & Gutkin, 2017) as predicted analytically by Cannon et al. (1983). Taken together an interneuron received 70.3 ± 13.5 $GABA_AR$ synapses. Only 8 % of the $GABA_AR$ synapses were located on the soma. The degree of correlated $GABA_AR$ input depended not only on the axonal overlap, but also on the coherence in firing among interneurons (hence on the circuit dynamics) and will be dealt with in Section 7. Finally adjacent interneurons were also coupled via 11.2 ± 1.6 electrical synapses on secondary and tertiary dendritic compartments.

As for the synaptic strengths, it is important to note that, in accordance with cerebellar physiology (for references see Maex & Gutkin, 2017), the AMPAR synapses were strong (1.8 nS peak conductance) so that a single spike could fire the interneuron. The $GABA_AR$ synapses were fast and strong as well, with a latency of 1.6 ms, a decay time-constant of 3 ms, and a peak conductance of 2.8 nS, generating postsynaptic currents of 12.8 pA peak amplitude on average. The electrical synapses were resistors of 200 pS conductance, but because the connected dendrites

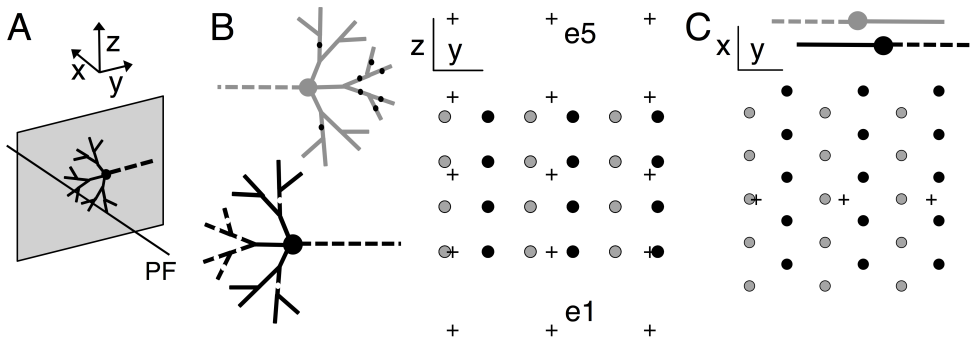

Figure 1: Organization of the interneuron circuit model. (A) The molecular layer of cerebellar cortex is dominated by excitatory parallel fibers (PFs) running parallel to the transverse (x) axis and orthogonally to the dendritic trees of the interneurons, which are confined to parasagittal (y-z) planes (grey). (B) and (C) View of the circuit projected on a sagittal (y-z) (B) and horizontal (x-y) plane (C). Populations of rostrally (anterior) and caudally (posterior) projecting inhibitory interneurons (grey and black, respectively) had their somata located in four layers (B), each layer organized as a hexagonal grid (C). Note that further randomizing the positions did not affect the results (Maex & Gutkin, 2017). Together, 800 interneurons (2 x 5 x 10 x 4) occupied a 100 x 720 x 220 μm volume (x x y x z) of cerebellar cortex. The axons, not modelled explicitly but represented as a short dashed line, made connections in the sagittal direction up to $>$ 200 μm from their origin. Toroidal connections were allowed to reduce boundary artifacts. In the fully coupled circuit neurons were also connected via dendrodendritic gap junctions (their positions on the dendritic tree indicated by small circles). Only the soma had voltage-gated channels, the dendrites (diameter 0.4 μm; full width 86 μm) were passive. The positions of the virtual electrodes are indicated by crosses. Scale bars in B and C measure 20 μm.

were very thin (0.4 μm diameter) spikes were hardly transmitted, generating only spikelets of sub-millivolt amplitude. In accordance with this, the effect of gap junctions was always to decrease the spike rate of the circuit, and their contribution to synchronization was smaller than that of shared excitation and inhibition (see Fig. 8, B and C, in Maex & Gutkin, 2017). Only in the absence of peripheral excitation were the electrical synapses essential for synchronization (see Section 6.3).

All connections were laid stochastically, and further heterogeneity was introduced by randomizing, between -54 and -52 mV, the reversal potentials of the neuronal leak currents (E_{leak}). All input fibres generated stationary Poisson spike trains of the same rate (5 s^{-1} except when stated otherwise).

2.2 Simplified models

The power spectrum of the LFP reflects the interaction of two factors: first, the spectrum of the active current sources and sinks generated by the neuronal membranes and, secondly, the (mostly passive) filtering by synapses, dendrites, and the intrinsic circuit dynamics. In order to

circuit model	AMPA currents	GABA currents	active currents	gap junctions
1. passive disconnected	+	-	-	-
2. active disconnected	-	-	+	-
3. active connected	+	+	+	+

Table 1: Circuit models and their currents

dissect these different components and the underlying currents, three versions of the interneuron circuit were simulated, and the raw LFP signals were compared to those obtained from the individual currents.

These three models were (see Table 1):

1. a circuit of passive neurons driven by excitatory synapses (simulated in Figs. 2 and 3),
2. a circuit devoid of synaptic input but with its neurons spiking spontaneously (Figs. 4 and 9 A, C and D),
3. the fully connected circuit with lateral inhibition and electrical coupling (Figs. 5, 6, 7, 8 and 9 B and E).

3 Calculation of the local field potential

According to Maxwell's theory all electric current entering the closed surface of a cell membrane must also instantaneously leave the cell (Gratiy et al., 2013). This current balance is the basis of all biophysical neuron models. For instance when an excitatory synaptic current depolarizes the neuron membrane, this charge accumulation at the membrane capacitor constitutes an outward displacement current that contributes to the LFP.

Hence, charge conservation requires that for each isopotential compartment the following current-balance equation holds:

$$I_{capacitive} + I_{leak} + I_{ligand} + I_{active} + I_{gap} + I_{axial} + I_{inject} = 0 \tag{1}$$

where the component currents are: the capacitive membrane current:

$$I_{capacitive} = C_m \frac{\mathrm{d}V}{\mathrm{d}t}, \tag{2}$$

the leak membrane current:

$$I_{leak} = g_{leak}(V - V_{leak}), \tag{3}$$

currents through ligand-gated channels:

$$I_{ligand} = \sum_i g_i(t)(V - V_i), \tag{4}$$

and currents through voltage-gated channels:

$$I_{active} = \sum_j g_j(t, V)(V - V_j). \tag{5}$$

Lastly, I_{gap} represents the current through electrical synapses, I_{axial} the axial currents between the compartments in the cable model of a neuron, and I_{inject} any externally applied current.

The actual membrane current I_m, which is the source of the LFP, has a resistive component I_{ion},

$$I_{ion} = I_{leak} + I_{ligand} + I_{active} \tag{6}$$

and a capacitive component, so that, combining (1) and (6),

$$I_m = I_{capacitive} + I_{ion} = -(I_{gap} + I_{axial} + I_{inject}) \tag{7}$$

From Eq. (7) it is clear that in multi-compartmental neurons with many ion channels, it is more practical to calculate the membrane current from the axial current, corrected for junctional and applied currents.

The LFP measures the total membrane current generated by all neurons in the circuit, attenuated by the extracellular resistance and hence inversely proportional to distance (Plonsey, 1964; Nunez, 1981). Inward and outward membrane currents are taken with negative and positive sign, respectively. By summing over all membrane currents I_m in the circuit, the LFP can be calculated, following Plonsey (1964) and Nunez (1981, eq. 3.15), as:

$$\Phi(\vec{r}, t) = \frac{1}{4\pi\sigma} \sum_{i=1}^{n} \frac{I_m^i(t)}{R_i}, \tag{8}$$

where R_i is the distance between the position $\vec{r}$ of the electrode and the centre of the ith compartment delivering current I_m^i. The scalar tissue conductivity σ was set to 0.25 S m^{-1};

anisotropies in conductivity (Nicholson & Freeman, 1975) were not taken into account.

In the present study, the LFP signal was also dissected into its component currents (strictly speaking: voltages) by substituting each of the membrane currents (ligand-gated, voltage-gated, leak and capacitive) separately for I_m in Eq. (8).

3.1 Simulation details

The models were built and simulated with Genesis 2.3 (Wilson & Bower, 1989). Because the present study started from a slightly earlier version of the model than that described in Maex & Gutkin (2017), for consistency this earlier version was used all through; it differed only by a lack of randomization of the neuron positions, and the use of a broader connection kernel along the transverse axis (60 vs. 40 μm). The LFPs were calculated from the axial currents (Eq. 7), using Crank-Nicolson numerical integration of the circuit dynamics in 20 μs steps (Van Dijck et al., 2012). As a test for numerical accuracy, the capacitive current was calculated by differencing the traces of membrane potentials and compared to that obtained by subtracting all ionic membrane currents from the LFP.

Except when otherwise stated, LFPs were sampled for 204.8 seconds at 60 μs intervals. The power spectrum estimation was calculated across sliding windows of 131076 points (7.86 s), each window mean-subtracted and smoothed with a Hann filter. The power spectra are standard normalized, such that total power equals the mean squared signal, in accordance with Parseval's theorem (Press et al., 2007).

3.2 A comment on the sign of the LFP signal

For a membrane current to generate an LFP, it must leave the neuron at a different distance (from the electrode) than that it entered. Obviously this is almost always the case when a multi-compartmental neuron receives synaptic input on its dendrite or generates action potentials at its soma. Inhibitory circuits, however, being composed of small neurons with varying orientations, cannot generate aligned arrays of dipoles that through positive interference amplify the LFP signal, as for instance pyramidal neurons in neocortex do.

How the currents combine to form the LFP is shown in Fig. 2 for a passive two-neuron circuit. The two interneurons have their dendrites running in opposite directions. Although an electrode sees outward current as positive, the sign of the LFP will depend on the direction of intraneuronal current flow. After activation of a peripheral synapse on the left neuron (position a), most of this inward current must leave the neuron at positions that are closer to the electrode

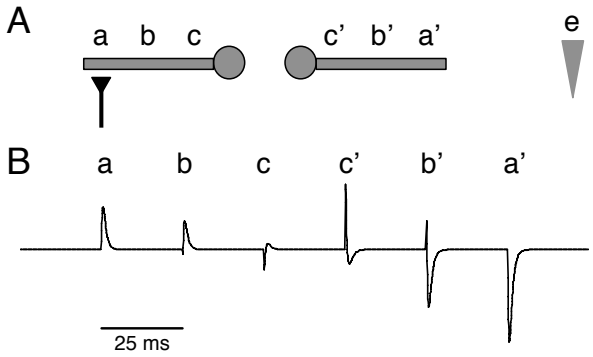

Figure 2: Local field potentials generated in a simplified circuit of two passive interneurons. (A) Schematic of the simulation setup: at 25 ms intervals an AMPAR synapse was activated either at position a, b, or c of the first neuron, which had its dendritic tree oriented centrifugally from the electrode located at (e), or at position c', b' and a' on the second neuron, whose dendritic tree was centripetally oriented. (B) Corresponding LFP traces recorded by electrode at (e).

than the point of entrance. Hence the outward current is less attenuated by distance than the inward current, and the LFP signal is predominantly positive. For synapses closer to the soma (positions *b* and *c*), part of the inward current travels towards to periphery of the dendrite, as can be seen from the brief negative deflection preceding the peak. Activation of synapses on the second neuron (positions *c'*, *b'* and *a'*) produces currents of opposite polarity, which in addition had a greater amplitude because the neuron was closer to the electrode.

4 First model: a population of passive neurons driven by excitatory synapses

In this first simplified model, the circuit was driven by spikes from PFs that activated (were filtered by) AMPAR synapses. Because the neurons were passive, they did not generate spikes, hence this circuit was disconnected. Since the input was a stationary Poisson process with flat power spectrum (He, 2014), this model can be used to assess the filtering properties of the passive components.

The continual input via AMPAR synapses generated a strong inward current that left the interneurons first as a low-frequency leak current of about the same magnitude (Fig. 3A) and secondly as a high-frequency capacitive current (Fig. 3C) of zero mean amplitude. These three currents were the only membrane currents, and together they formed the LFP signal. Figures 3, B and D, show the power spectrum of the LFP signal, and its dissection into the component membrane currents.

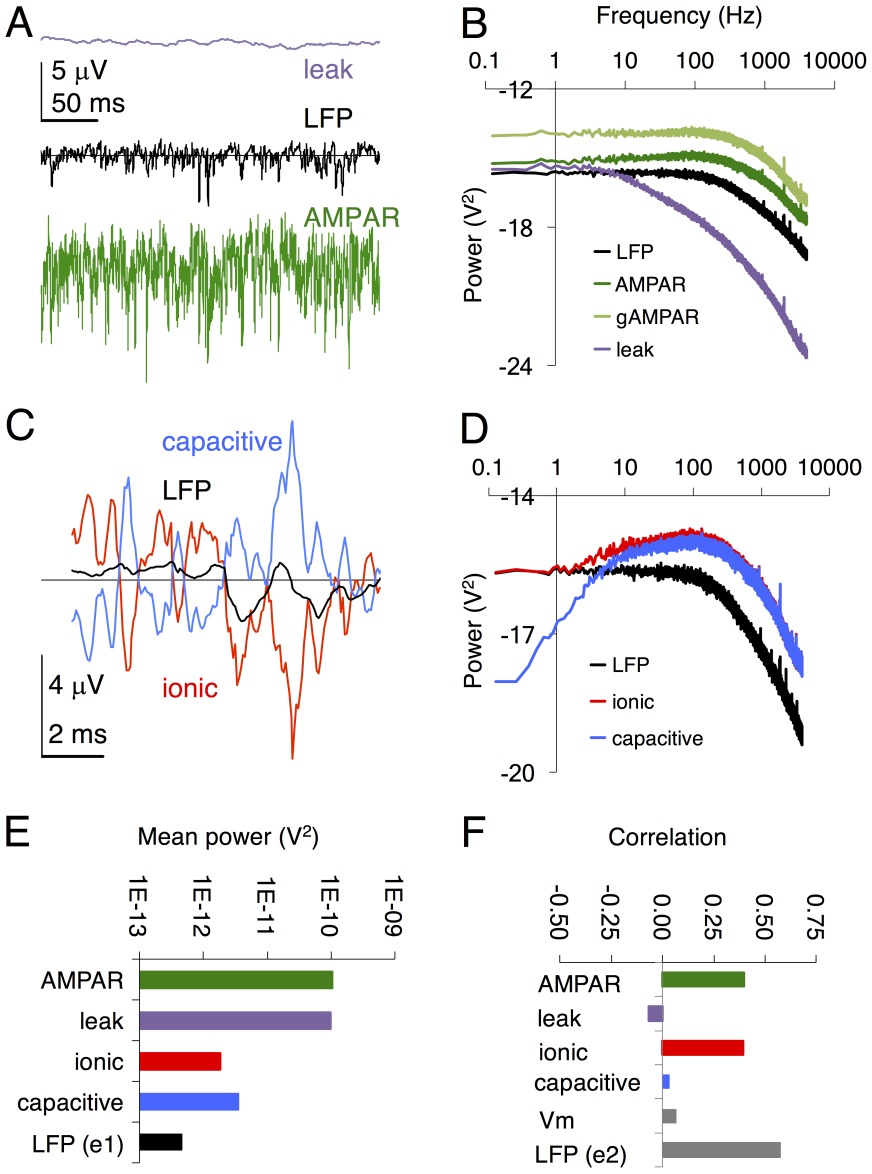

Figure 3: The local field potential and its current components in a population of passive neurons driven by excitatory synaptic input (Model 1). The afferent spike trains had a flat spectrum (not shown). (A) Sample traces of the LFP (black), leak current (purple) and AMPAR current (green). (B) Power spectra of the currents from A, and of the AMPAR conductance (light green in arbitrary units, overlaid for comparison). (C) Sample traces of the LFP (black), total ionic membrane current (red, AMPAR + leak, see Eq. 6) and capacitive membrane current (blue). (D) Power spectra of the LFP and underlying currents from C. (E) Average power (on logarithmic scale) of the LFP and its individual current components, calculated at electrode position e1 in Fig. 1B. (F) Correlation of each current component with the LFP signal. The autocorrelation measures 1. Entry Vm measures the correlation between the LFP and the compartmental membrane potentials. The last entry is the correlation of the LFP signal at e1 with that at e2, an electrode at 30 μm distance.

The synaptic AMPAR was a two-stage linear low-pass filter (Freeman & Zhai, 2009; Wilson & Bower, 1989), with rise and decay time-constants of 0.03 and 0.5 ms, respectively. The power spectrum of its conductance trace during a simulation, plotted (in arbitrary units) in Fig. 3B above that of the LFP contribution of the AMPAR current, falls off with a maximum slope of about -4, as expected for a second-order filter. The leak current, which scales with the membrane potential (Eq. 3), underwent a further low-pass filtering by the membrane RC circuit, and has a corner-frequency (halving of signal amplitude) at about 14 Hz (Fig. 3 B), whereas the power of the capacitive current rises with frequency up to about 100 Hz (Fig. 3 D) (Bracewell, 1965). Taken together, the LFP signal (black trace) is low-pass with a corner-frequency of about 300 Hz.

Note that the LFP has a power less than that of any of its individual current components (Fig. 3E). The reason is that especially the high-frequency currents cancel each other. For instance, the high-frequency component of the AMPAR current is almost completely balanced by the capacitive current in Fig. 3C, indicating that it leaves the compartment of entry as a displacement current instead of being axially propagated along the narrow dendrites. On the power spectrum, consequently, the LFP lacks the high-frequency component present in the ionic and capacitive currents (Fig. 3D). Overall, the only current that correlates well with the LFP signal of this passive model is the synaptic AMPAR current (Fig. 3F) (see also Mazzoni et al. (2015)).

5 Second model: a population of spontaneously active neurons

In this second simplified model, the circuit was an uncoupled collection of spontaneously active neurons. This circuit enables one to assess the power spectrum of the active components, besides the ever present leak and capacitive currents.

Adding voltage-gated channels to a passive compartment tended to hyperpolarize its membrane so that the leak current, contrary to its action in the passive model, became inward (Fig. 4A). Depending on the strength of their leak current (E_{leak} was randomized between neurons), the neurons could act as pacemakers and spontaneously generate spikes. In the population of 800 interneurons, this spontaneous spike rate was between 0 and 14 spikes s^{-1} (mean 7.95 $\pm$ 3.84, with 35 neurons remaining silent).

The strongest voltage-gated currents were generated by the fast inactivating Na channel

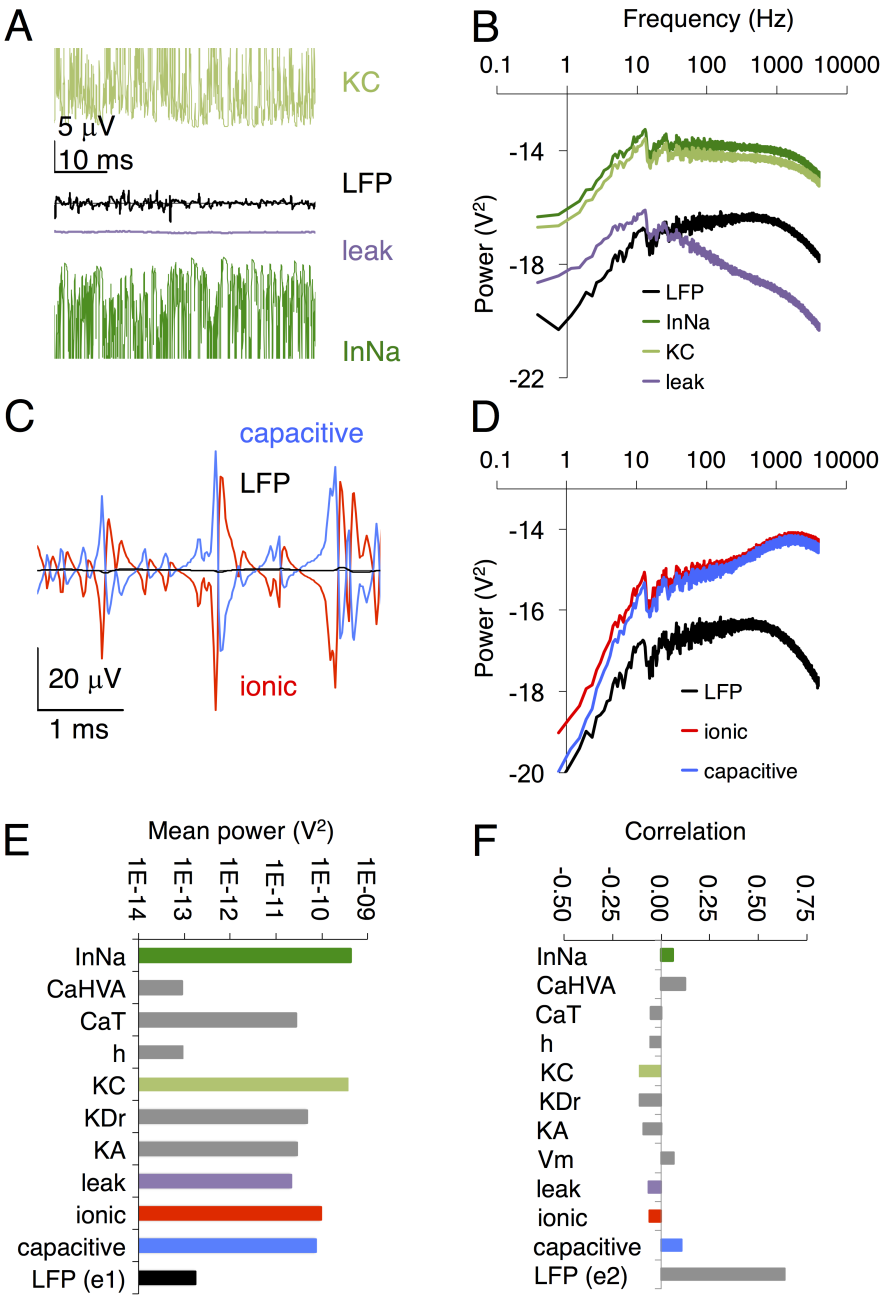

Figure 4: The local field potential and its individual current components in a population of spontaneously active neurons (Model 2). Same format as in Fig. 3. In A the peaks of the LFP components from the InNa (green) and KC (light green) currents have been truncated at ± 30 μV. For channel names, see section 2.1.

(InNa), which initiated the spike, and by the voltage- and Ca-dependent BK channel (KC), which repolarized the soma membrane (Fig. 4, A and E).

Owing to the absence of low-pass filtering by AMPAR synapses, which dominated the power spectrum in the passive model, the LFP power in the active model peaks between 100 and 1000 Hz (Figs. 4, B and D). As in the previous model, though, the LFP had less power than most of its current components (Fig. 4E), which partly cancelled one another (Fig. 4C). Neither was any of the individual currents strongly correlated with the LFP signal (Fig. 4F).

6 The synaptically connected interneuron circuit

Combining the previous two models yields the full, AMPAR excited, laterally inhibitory circuit. This version also had gap junctions, a typical feature of many inhibitory circuits, and although their currents do not contribute to the LFP, they may change the circuit dynamics and must be taken into account when the membrane current is calculated using Eq. (7).

Figure 5A compares the power spectra of the LFPs in the three circuits. Compared to the passive circuit, whose power spectrum is almost flat below 100 Hz (dark green curve), there is an increase in power from 100 down to 10 Hz and an even steeper increase below 10 Hz (light green curve). Fitting the spectrum with power functions f^n lets distinguish different frequency regimes, the exponents n (slopes on log-log plot) of which are indicated in Fig. 5C. Averaged over all 40 electrodes in the circuit, the mean slopes and their standard deviations were: -0.99 $\pm$ 0.16 (0.1–10 Hz; maximum of -1.257 at e3), -0.33 $\pm$ 0.08 (10–100 Hz), -1.34 $\pm$ 0.24 (100–1000 Hz) and -2.63 $\pm$ 0.25 ($>$ 1000 Hz).

The steep fall-off beyond 1000 Hz with $n \approx$ -3 was caused by synaptic AMPAR filtering, as it was already present in the passive circuit. The $1/f$ scaling at the lowest frequencies is a new feature of the circuit to be dealt with below. The hump in the 30–100 Hz γ-frequency range must be attributed to regenerative membrane currents and spiking activity, as its power increased with the level of excitation (Fig. 5B). Note also that in the absence of excitatory input, the circuit completely changed its dynamics and generated α-frequency oscillations (orange curve in Fig. 5B).

We will now discuss in greater detail the behaviour of the circuit within each of these different frequency regimes.

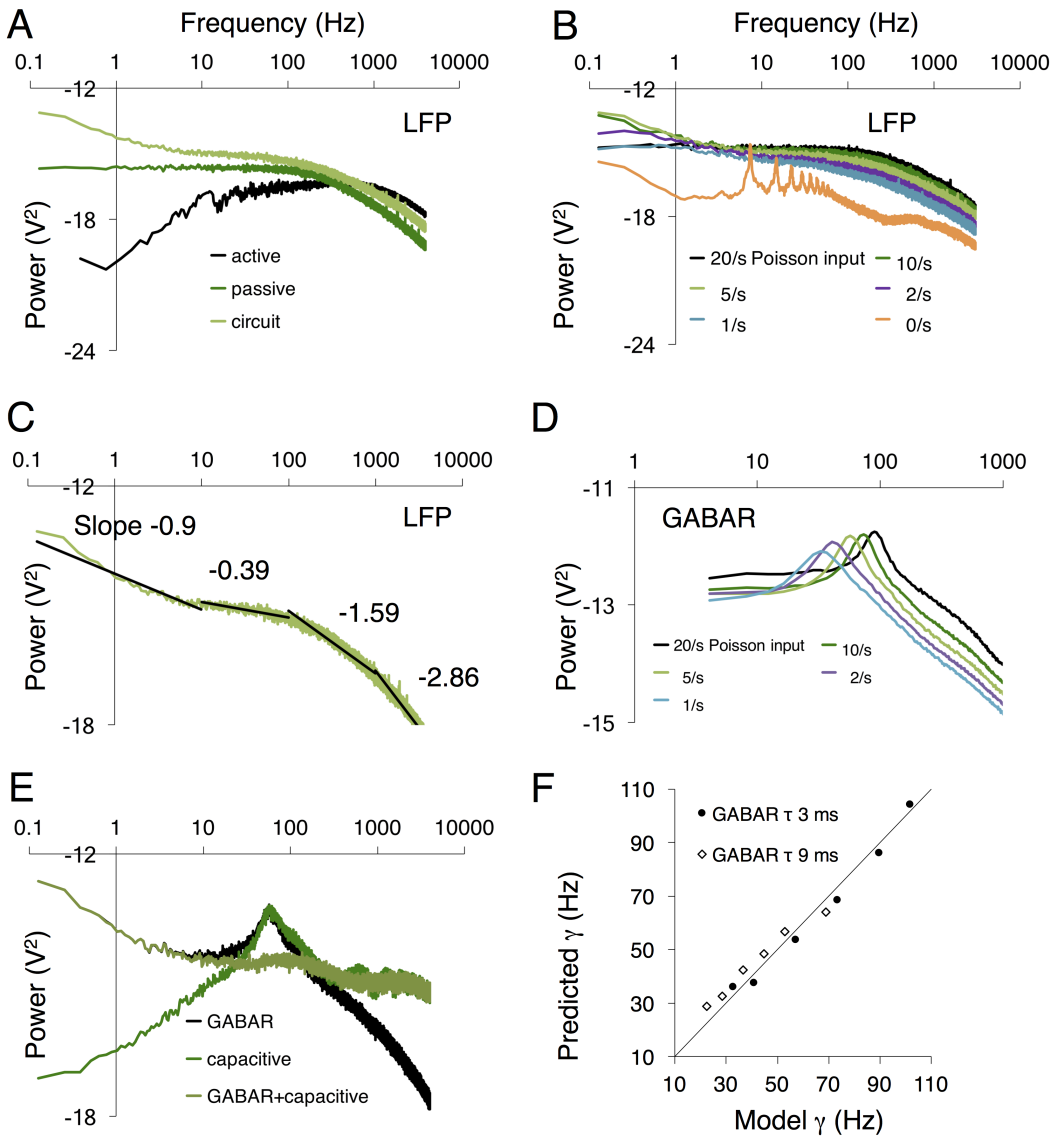

Figure 5: Local field potentials in the full circuit model (Model 3). (A) Comparison of the power spectrum of the full-circuit model with that of Models 1 (passive circuit) and 2 (active but disconnected). (B) Comparison of the power spectrum of the circuit model at the default level of excitation (stationary 5 s^{-1} Poisson input) with that at lower and higher levels of excitation. (C) Piecewise fitting of the spectrum by functions f^n of indicated slope n. (D) Power spectra of the LFP components generated by the $GABA_AR$ current when the circuit was stimulated at the indicated rates. (E) Isolation of the power spectra of the $GABA_AR$ component, the LFP component made up by the capacitive current, and the signal obtained by summing these two current components. (F) Comparison of the γ frequency, as measured from panel D, with that predicted from formula 9.

6.1 Accumulation of power in the γ band

Increasing the strength of peripheral excitation enhanced the power selectively in the γ range, flattening the spectrum between 30 and 100 Hz, its slope n diminishing from -0.67 (1 s^{-1} Poisson input) to -0.39 for the default circuit (5 s^{-1} input, Fig. 5C) to becoming almost flat (slope -0.16) for 20 s^{-1} input (Fig. 5B). A similar slope reduction in the 10-100 Hz domain has been found in human electrocorticograms during visuomotor tasks (Podvalny et al., 2015), and in a study modelling the effect of excitation-inhibition balance (Gao et al., 2017). In the passive model, in contrast, changing the spike rate of the input fibres would merely shift the power spectrum up or down.

This γ plateau is even more conspicuous in the power spectrum of the $GABA_AR$ component where a clear γ peak arises (Fig. 5D). As the $GABA_AR$ current is the convolution of the unitary synaptic conductance with the afferent spike trains, a γ peak must also be present on the power spectrum of the spike trains, as shown in Fig. 6A for another realization of the circuit (taken from Maex & Gutkin (2017)). In the full LFP signal, however, this $GABA_AR$ peak became almost completely occluded by the capacitive current component (dark green curve in Fig. 5E).

The position of the γ peak in Fig. 5F ranged from 33 Hz for a circuit with a mean interneuron spike rate of 1.3 s^{-1} (range 0.2–4.7, generated with 1 s^{-1} Poisson input) to 102 Hz for a circuit with a mean spike rate of 33.5 s^{-1} (range 0–246, generated with 40 s^{-1} input). Apart from the degree of circuit activity, another determinant of the position of the γ peak was the decay time-constant of the $GABA_AR$ conductance (Wang & Buzsáki, 1996). Overall the position of the γ peak was well predicted by the following formula

$$f = \frac{1}{d + \tau + m} \tag{9}$$

where d is the fixed connection delay of 1.6 ms, τ is the decay time-constant of the $GABA_AR$ conductance (3 or 9 ms in Fig. 5F), and m is the most frequent inter-spike interval (ISI), hence the modus of the ISI histogram. The rationale behind this formula is that, first, the γ frequency is much better predicted by the modus of the ISI distribution than by its mean, especially at low spike rates (at high rates the modus and mean almost coincide). For instance, at an average input rate of 1 s^{-1}, the interneurons displayed ISIs with a modus of 20.4 ms, corresponding to an instantaneous spike rate of 49 s^{-1}, despite the average interneuron spike rate being only 1.3 s^{-1}. Whereas m is a metric for the fastest ISIs of individual neurons, the delay parameter d defines the interval within which different neurons can safely synchronize their spikes before

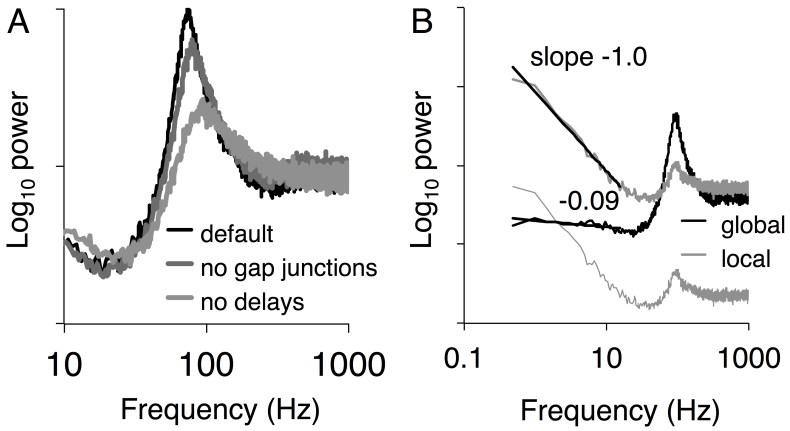

Figure 6: Spike-train analysis of the full model. All power spectra (in arbitrary units, ticks on vertical axes indicate factors of 10) were calculated from spike-time histograms (bin-width 1 ms) averaged over 4096-ms windows. (A) Simulations of the realization of the model used in Maex & Gutkin (2017), with a Poisson input rate of 10 s^{-1}. As explained in section 2.1, the default model had 200 pS gap junctions and 1.6 ms connections delays. B. Spike-train power for the simulation with 20 s^{-1} input of Fig. 5. The power spectrum was calculated either across all 800 interneurons (black trace), or over a local subset of 40 interneurons (grey curves). The power of the local subset (lower grey curve) was re-normalized into the upper grey curve to compensate for its smaller number of spikes.

inhibiting one another (Maex & De Schutter, 2003). The parameter τ, finally, accounts for the well-known effect of the $GABA_AR$ kinetics (Wang & Buzsáki, 1996). The position of the γ peak hardly depended on the strength of inhibition, as this very little affected the modus of the ISI histogram.

Note that even in an uncoupled circuit, individual interneurons showed a peak on their power spectrum centred at $1/m$ owing to their refractory period, as predicted by analytical studies (Franklin & Bair, 1995; Schwalger et al., 2017). It is clear, however, that any parameter that enhanced the synchrony among the neurons would also substantially increase their γ power. Examples are not only inhibitory coupling, but also shared excitation and connection delays. A delay on the (inhibitory) connections as small as 1.6 ms enhanced the power (amplitude) by a factor greater than 4 (2) (Fig. 6A). In the absence of electrical coupling the γ power decreased by 36 % (Fig. 6A) but without affecting synchronization (see Fig. 8 B in Maex & Gutkin (2017)), in accordance with experiment (Hormuzdi et al., 2001; Neske & Connors, 2016). In the present simulations, the spike rates were too low to evoke the additional resonance peak at $1/4d$ or 156 Hz predicted by Maex & De Schutter (2003).

We would refrain, however, from calling this concentration of power in the γ band a genuine γ oscillation or a γ rhythm for two reasons: first, although nearby neurons strongly synchronized,

there were no signs of rhythmicity on the auto- or cross-correlogram, apart from the refractory period (see Fig. 8B in Maex & Gutkin (2017)) and, secondly, at all levels of excitation the neurons fired almost as irregularly as Poisson spike trains with a CV2 > 0.8. It was only during transients, such as after the pause in Fig. 7, that a clear γ rhythm was discernible lasting about 100 ms.

6.2 $1/f$ power scaling at low (< 10 Hz) frequencies

We attribute the amplification of low-frequency (0–10 Hz) power to low-pass filtering through a well-known mechanism of gradual self-disinhibition, mathematically equivalent to self-excitation (Cannon et al., 1983). Indeed, the exponent of -0.9 in Fig. 5C became less negative when the strength of inhibition was reduced (see Fig. 9 in Maex & Gutkin (2017); this study also demonstrated other signs of low-pass filtering such as phase-lagged responses to sine-wave stimuli, and tonic response components to pulses).

The absence of low-frequency $1/f$ power scaling in some of the spectra of Fig. 5B is only apparent, for two reasons. First at this electrode depth (e1 in Fig. 1B) the power was dominated by the massive PF input on the dendrites. A second explanation is provided in Fig. 6B, where spectral analysis of the spike-time histogram showed a very prominent $1/f$ scaling when power was calculated across only a local sub-population of interneurons, but a flat low-frequency spectrum when calculated across the entire circuit. The reason is that strong lateral inhibition forced sub-populations to fire in anti-phase (see rasterplot in Fig. 7A), canceling their contributions to the power spectrum except when power was calculated very locally.

6.3 Spontaneous α oscillations in the absence of peripheral excitation

A new finding of the present study is that the dynamics of the interneuron circuit completely changed when the Poisson excitatory input was abolished. In the absence of excitation, the dynamics was dominated by spontaneous synchronous oscillations at α frequencies (from 7.4 Hz in Fig. 5B to 12.7 Hz in Fig. 7). These α oscillations required the interneurons to be coupled electrically, but not chemically. The frequency of 7.4 Hz in the default circuit could hardly be manipulated by changing the strength or time-constant of the $GABA_AR$ synapses. For instance, with inhibition reduced to 20 % the frequency still measured 7.8 Hz. Changing the decay time-constant from 3 ms to 9 or 2 ms changed the frequency only from 7.4 Hz to 6.1 and 7.8 Hz, respectively. Even with all inhibition blocked a strong α rhythm of 12.2 Hz persisted for an average spike rat of 12.6 ± 0.9 s^{-1}, close to the *intrinsic* spike rate (or pacemaker rate) of the

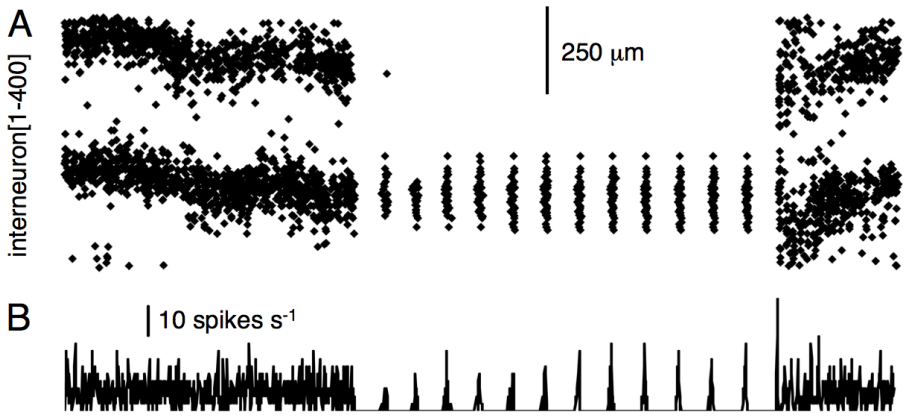

Figure 7: Transition from γ power to α oscillations during a 1 s pause in excitation. Before and after this interval, all input fibers spiked randomly at a rate of 5 s^{-1}. In this simulation, the frequency of the α rhythm was increased to 12.7 Hz by extending the randomization interval for E_{leak} from [-54, -52] mV to [-54, -49] mV. (A) Rasterplot of spikes; for clarity, only one half of the interneurons ([1–400]) are shown. The spatial patterning of activity was a consequence of the strong lateral inhibition. (B) Spike-time histogram over the entire circuit of 800 interneurons (binwidth 1 ms).

fastest neurons in the uncoupled circuit (13.8 s^{-1}).

These presumed α oscillations were very sensitive, however, to the density of electrical coupling between the interneurons, their power falling to 4 % when half of the gap junctions were deleted. Since in the absence of external stimulation, the interneurons' leak potential was their driving force, the most important parameter determining the α frequency was the average *intrinsic* spike rate of the interneurons. Hence the α frequency increased from 7.4 Hz to 12.7 Hz when the intrinsic spike rate (measured in the uncoupled circuit of Model 2) rose from 7.95 to 15.6 spikes s^{-1}. Figure 7 shows an example of the rapid switching from γ power to a 12.7 Hz α rhythm when the PF input was silenced.

The slowest rhythm that could be maintained by this mechanism had a frequency of 6.4 Hz for an average intrinsic spike rate of 5.3 s^{-1}; at the upper side there was in principle no limit. Note also that the interneurons fired during the α rhythm at a lower *average* spike rate than when they fired asynchronously in a circuit devoid of gap junctions (0.31 versus 0.87 s^{-1}), as spiking by a fraction of them (5–10 %) sufficed to entrain the rhythm, and because gap junctions tended to decrease the spike rate, as mentioned above.

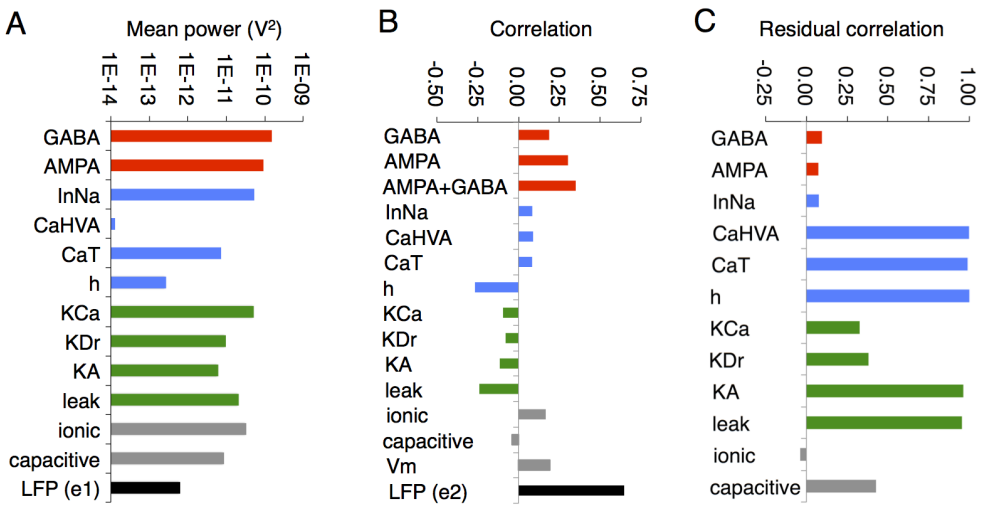

Figure 8: Contribution of individual membrane currents to the local field potential in the full circuit model (Model 3). (A) Average power (on a logarithmic scale) of the LFP and its current components. (B) Correlation of each current component with the LFP signal. (C) Correlation between the full LFP signal and the proximate LFP signal that was generated by subtraction of the indicated current.

6.4 Co-occurrence of power in the different frequency bands

As shown in Fig. 5B, the $1/f$ scaling below 10 Hz can coexist with the α rhythm and with power in the γ band. Notice in Fig. 6B how the power moved from the γ band to slow frequencies, depending on the spatial resolution of the recording. A shallow γ peak was also present during the α rhythm, but its power was so much smaller than that of the α rhythm (and its harmonics) that it would go unnoticed.

6.5 Currents underlying the LFP signal

Most of the contributing currents to the LFP signal had a power an order of magnitude greater than that of the LFP itself (Fig. 8A). The voltage-gated currents had a total power about half that of the synaptic currents, which is less than in a biophysical neocortex model (Reimann et al., 2013) but can be attributed to the use of passive dendrites in the present interneuron model. Their *variance* even accounted for 77 % of the variance of the LFP.

The sign of the correlation of the individual currents with the LFP signal at electrode e1 (Fig. 8B) followed a simple rule: inward currents that were activated during (or associated with) depolarization, as well as outward currents associated with hyperpolarization, had a positive correlation with the LFP, the others (for instance the outward K currents activated during depolarization) were negatively correlated. The LFP correlated also fairly well with the (inverse-

distance-weighted) membrane potential Vm (19.2 % versus 18.8 % for the correlation with the $GABA_AR$ current), a phenomenon also observed in mouse visual cortex (Haider et al., 2016).

Correlation was a bad metric for assessing the contribution of a single current to the LFP, however, as currents with very little power, such as the h-current, had among the highest correlations (-0.27). We therefore calculated in Fig. 8C how much the LFP signal would deteriorate if a particular current were ignored. Omitting the synaptic currents ($GABA_AR$ and AMPAR) or the spike-generating sodium current (InNa) almost completely destroyed the LFP signal, reducing the residual correlation to less than 10 %. Many other currents (such as CaHVA, CaT, h, KA) were too weak to have an appreciable effect, but the high-frequency capacitive current nevertheless was needed to maintain a correlation of more than 50 %.

7 Frequency dependence of the spatial propagation of the LFP

Coherence (Thomas, 2015; Nunez, 1981) between the LFP signals computed at different electrode locations may result from passive propagation of the LFP in the resistive extracellular medium, or from spatial correlations in the membrane currents (through the spatial extension of the dendrite, shared external inputs, or circuit-driven synchronization). We used the three different models to examine these mechanisms.

Figure 9A compares the LFP signals recorded at five depths (see Fig. 1B) in the spontaneously active model. The neurons of this circuit, lacking synaptic input, fired rhythmically (at varying frequencies) but completely desynchronized. The coherence declined above a corner frequency of about 500 Hz, sufficient to attenuate the extracellular action potential more strongly with distance (panel C) than its component InNa current (panel D). The latter current, like all other currents, fell off inversely with distance (Eq. 8). Since the extracellular medium was purely resistive, any effect of temporal frequency on the propagation of the LFP signal must have been a consequence of filtering by the neurons themselves, implying that high-frequency signals such as action potentials generate smaller dipole moments, as predicted by cable theory and a model by Lindén et al. (2010).

The most remarkable feature in the full circuit was an enhanced coherence at low frequencies (< 20 Hz) (Fig. 9B). This coherence followed a spatial profile, illustrated in panel E, coinciding with the pattern of alternating bands of active and inactive interneurons seen along the sagittal axis in Fig. 7A. This pattern had a spatial wavelength of 360 μm (half the circuit length), and

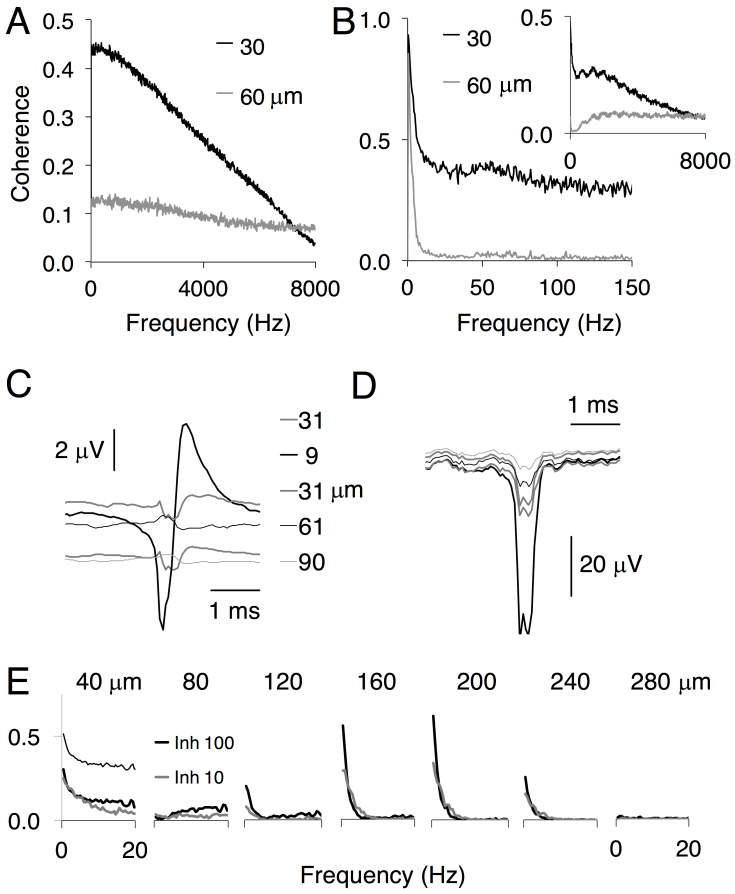

Figure 9: Attenuation of the LFP signal with distance. (A) Coherence function of the LFP between pairs of electrodes that were 30 μm (black) or 60 μm (grey) apart along the z-axis in the active but disconnected circuit (model 2 of Table 1). (B) Coherence for the fully connected circuit (model 3). (C) Spike-triggered LFP at electrodes located at the indicated distances from the source neuron in model 2. (D) Same potentials as in C, but generated exclusively by the sodium (InNa) current. (E) Coherence in the low-frequency range (< 20 Hz) averaged over all horizontal pairs of electrodes separated by the indicated distances along the sagittal (y-) axis of the full-circuit model 3. Thick black and grey traces were from simulations with full inhibition, and inhibition reduced to 10 %, respectively. In all traces but the upper one in the first panel, the coherence already present in the passive model (model 1) was subtracted. Beyond 40 μm this passive coherence was negligible and its contribution is no longer shown.

the resulting coherence function in Fig. 9E was maximal at electrode separations equal to half this period (hence between the sites of active and silenced neurons), and minimal at quadrature phases. The coherence was dependent on the strength of inhibition, being halved when inhibition was reduced to 10 % (grey curves in Fig. 9E). Only at the shortest electrode distance (40 μm, first panel of E) may part of the coherence have been generated by overlap of the dendrites and shared excitation, as a short-distance coherence was already present in the passive synaptically driven circuit (see difference between thin black trace, plotting the raw coherence, and thick trace obtained after subtraction of the passive-model coherence).

It has been shown that in model pyramidal cells a strong polarity in the location of correlated inputs may increase the slope of the power by recruiting dendritic low-pass filtering (Łeski et al., 2013). In the present compact interneurons (90 μm path length from soma to dendritic tip), however, locating all the $GABA_AR$ synapses on the soma did not add any low-pass filtering. The slope of the LFP power at low frequencies even decreased on average from -0.99 to -0.72, but this decrease was completely on account of the outmost electrodes (e1 and e5 in Fig. 1B), which now recorded from bare dendrites. At the central electrodes, located closest to the somata, the slope was still -0.91 on average. In brief, reciprocal inhibition itself generated a slowly correlated activity in the circuit, without much contribution of dendritic filtering.

8 Discussion

The present results confirm and extend the study by Wang & Buzsáki (1996) on the emergence of fleeting γ-frequency oscillations in interneuron circuits, and predict further that such circuits may be involved in generating other spectral characteristics, such as a $1/f$ power scaling and the α rhythm. The model was based on the architecture and electrophysiology of the circuit of inhibitory interneurons in the molecular layer of the cerebellar cortex (Maex & Gutkin, 2017), but it is noteworthy that all spectral properties reported here were post-hoc findings which the model had not been tuned for.

In brief, in this purely inhibitory circuit, the γ power was a consequence of the neuronal refractory period (Franklin & Bair, 1995), enhanced by synchronization. The $1/f$ scaling was a circuit phenomenon of lateral inhibition and disinhibition, and the strong α rhythm that emerged in the absence of excitation was generated by electrical coupling among intrinsic pacemaker neurons. As only a fraction of the interneurons (5–10 %) needed to spike to maintain this α rhythm (the mean spike rate dropped to < 0.5 s^{-1}), this rhythm may rather be an energy-saving brain mode.

8.1 Model constraints and predictions

Several characteristics of the circuit and its component neurons were essential for its rich spectral behaviour, and the extrapolation of the present findings to other circuits will primarily depend on the fulfilment of these constraints.

First, inhibition was strong with a predominance of lateral over self-inhibition. As shown in Maex & Gutkin (2017) and predicted by Cannon et al. (1983), the resulting slow disinhibition can enhance the integration time of the circuit to > 1 s, amplifying power selectively in the low-frequency domain, and shaping the $1/f$ power scaling.

Secondly, in the absence of synaptic AMPAR stimulation, the dense electrical coupling induced a synchronous α rhythm. This rhythm was driven by the intrinsic spiking (pacemaker) propensity of the interneurons, but slowed down by the electrical coupling between their very thin dendrites, which favoured transmission of slow (synaptic or afterhyperpolarization) potentials (see Fig. 8C in Maex & Gutkin, 2017).

Thirdly, unitary AMPAR synapses were strong enough to evoke a spike, which explains the rapid desynchronization of the α rhythm by random peripheral input (Fig. 7) and the consequential shift of power to the γ band.

The point-neuron circuit originally analysed by Cannon et al. (1983) has the remarkable property that reciprocally connected inhibitory neurons respond briskly to their shared inputs, but integrate differences in input with a slow time-constant. This behavior was confirmed in simulations of the present cerebellar circuit using sinewaves and pulses as stimuli (Maex & Gutkin, 2017). Pharmacologically blocking (enhancing) inhibition would therefore be predicted to reduce (increase) the circuit time-constant, at least if no feedback excitation is unleashed. This is in accordance with a recent re-analysis of ECoG data (Fig. 4A of Gao et al. (2017)), where a propofol-induced increase in $GABA_AR$-mediated inhibition was found to strongly enhance the slope of power below 10 Hz.

8.2 Extrapolation from cerebellar cortex to other brain regions

Interpreting the spontaneous cerebellocortical rhythms is particularly difficult, owing to the multitude of both peripheral and central inputs to cerebellar cortex and the high spontaneous activity of its principal neurons, the Purkinje cells (Bremer, 1958; Cebolla et al., 2016; Courtemanche et al., 2013; Middleton et al., 2008). On the other hand, it has been argued that cerebellar cortex and neocortex may generate the same rhythms independently (Niedermeyer, 2004). Given the abundance of electrically coupled inhibitory circuits in the brain (Hestrin & Galarreta, 2005; Lee

et al., 2014), it may be worth considering the present mechanisms for the spectral properties of other regions and of neocortex in particular, taking into account the obvious differences in synaptic organization. One of the major differences is the putative lack of recurrent excitation in cerebellar cortex. Most neuron types are inhibitory, and the excitatory granule cells do not make recurrent connections (an exception is made here for the unipolar brush cells). As a corrolary, studies on the balance between excitation and inhibition (Lombardi et al., 2017) may be less relevant for the cerebellum, as there is no need for inhibition to check feedback excitation.

Another remarkable difference is the strong anisotropy of the connections in cerebellar cortex. This difference, however, should not preclude a generalization of the present results, as the major parameter determining the circuit time-constant was the extent of lateral over self-inhibition (Maex & Gutkin, 2017), which can be varied using isotropic, radial connection kernels as well. Evidently, other forms of self-inhibition, such as spike-rate adaptation, are expected to reduce the time-constant and hence the slope of the power function at low frequencies. Candidate inhibitory neuron types for implementing slow temporal integration in neocortex would therefore preferentially be non-adapting, such as the fast-spiking basket cells in layers 2–6 and the late-spiking gliaform cells in layer 1. Each of these interneuron types forms micro-circuits coupled through chemical and electrical synapses (Chu et al., 2003; Tremblay et al., 2016).

8.3 Physiological relevance: interneuron control of brain rhythms

Even though interneurons themselves contribute probably little current to the LFP, owing to their compact morphology, symmetrical synapse placement, and the variable orientation of their dipole moments (Mazzoni et al., 2015), their effect on circuit dynamics is substantial. Physiological support for the involvement of inhibitory interneurons in the γ power may be found elsewhere (Buzsáki, 2006; Buzsáki & Wang, 2012). We here briefly discuss their potential role in the α rhythm and in $1/f$ power scaling.

Haegens et al. (2015) found α generators to be distributed across all layers of neocortex, and van Kerkoerle et al. (2014) suggested the rhythm may be initiated in layer 1, which is especially rich in electrically coupled interneuron circuits (Chu et al., 2003). The γ activity, in constrast, would initiate in layer 4, which receives monosynaptic excitation from thalamocortical cells (van Kerkoerle et al., 2014). In the present model, the γ frequency (Fig. 5F), but not the α frequency (Section 6.3), could easily be changed by (allosteric) modulation of the $GABA_AR$ channel, in agreement with experimental observations (Lozano-Soldevilla et al., 2014). A role for electrical coupling in α has further been suggested in the thalamus (Hughes et al., 2011). The α rhythm

is also known to recruit rhythmic inhibition that windows perception (Haegens et al., 2011).

The $1/f$ scaling at low frequencies (< 10 Hz) was already observed on the spike-train spectra in our previous modelling study (Maex & Gutkin, 2017) and is confirmed here for the LFP. Admittedly, $1/f$ scaling is ubiquitous in physical systems (Schroeder, 1991), and its interpretation often difficult (Stumpf & Porter, 2012). In brain signals the most straightforward explanation for an inverse relationship between amplitude and frequency is that synchrony of low-frequency signals is less sensitive to jitter over short delays (Gloor, 1985). Even so, this would generate a $1/f^2$ scaling of power, not the slopes close to -1 often observed in EEG and MEG recordings. Novikov et al. (1997) found mean slopes of -0.98 and -1.28 in the 0.4–40 Hz range of the MEG for a male and female subject. Dehghani et al. (2010), in a group of four subjects, found mean slopes of -1.33 and -1.06 in the 0.1–10 Hz range of EEG and MEG, respectively.

In the present model, $1/f$ power scaling below 10 Hz was generated through reciprocal inhibition (Cannon et al., 1983), and often coincided with spatial patterning of the spike-time rasterplot (Fig. 7), which may be thought of as a mark of travelling waves (Neske, 2016) and alternating UP and DOWN states (Schwalger et al., 2017). In modelling studies of pyramidal neurons, a $1/f$ power scaling (although at somewhat higher frequencies) has been attributed to dendritic filtering (Łeski et al., 2013), and to the activation of subthreshold currents such as the regenerative persistent sodium current (Ness et al., 2016). The origin of this $1/f$ power scaling is still unresolved, and many models take recourse to extra-neuronal mechanisms such as time-varying inputs (Barbieri et al., 2014), $1/f$ synaptic noise (Mazzoni et al., 2008; Pettersen et al., 2014), the superposition of different noise, relaxation or threshold processes (Rosen, 1972; Schroeder, 1991), or ionic diffusion in extracellular space (Halnes et al., 2016). Note also that the sole input to the present model consisted of stationary Poisson point processes, whose power was constant across frequencies (He, 2014), and that applying correlated inputs may further increase the slope of the spectrum (El Boustani et al., 2009; Łeski et al., 2013).

Last but not least, the randomness of the input used in the present study, the sensitivity of the slope to the strength of inhibition and the finding of correspondingly slow integration times in the responses to pulse and sine wave stimuli (Maex & Gutkin, 2017), seems to exclude that this $1/f$ scaling would be a finite-size artefact generated by the leakage of infra-cutoff frequencies into the spectrum (Lainscsek et al., 2017).

8.4 Interpretation of the LFP signal

The LFP is generated by many component membrane currents that partly cancel one another (Figs. 3E, 4E and 8A). Especially the high-frequency currents do not propagate axially along the dendrite but leave the neuron close to the point of entry as capacitive currents, generating smaller dipoles that more rapidly attenuate with distance to the recording electrode (Fig. 9A) (Lindén et al., 2010). Conversely, omitting the capacitive current in the calculation of model LFPs may generate grossly distorted LFP signals (Fig. 8C).

The present study suggests that the genuine LFP may underrate the γ power as compared to that derived form multi-unit spiking activity (compare Figs. 5B and 6A), a phenomenon also observed in a circuit model of excitatory and inhibitory leaky-integrate-and-fire neurons (Mazzoni et al., 2008). Admittedly, the γ peak may grow when principal neurons are added, in which synaptic positions are more polarized, and $GABA_AR$ activation generates larger, and better aligned, axial currents.

The present study also suggests that changing the spatial resolution of the recording method may profoundly change the spectral structure of the LFP signal. Too low resolution may shift low-frequency signals to the γ band (Fig. 6B). These low-frequency signals may constitute travelling waves of UP- and DOWN states (Neske, 2016; Schwalger et al., 2017), cancelling each other when sampled too diffusely. It is therefore tempting to attribute differences in the spectral structure of simultaneously recorded EEG and MEG signals (Dehghani et al., 2010) to putative differences in spatial resolution.

Acknowledgements

This work was partly supported by ANR-10-LABX-0087 IEC and ANR-10-IDEX-0001-02 PSL (France).

References

Abrahamsson, T., Cathala, L., Matsui, K., Shigemoto, R. & DiGregorio, D. A. (2012) Thin dendrites of cerebellar interneurons confer sublinear synaptic integration and a gradient of short-term plasticity. *Neuron*, *73*, 1159–1172.

Barbieri, F., Mazzoni, A., Logothetis, N. K., Panzeri, S. & Brunel, N. (2014) Stimulus dependence of local field potential spectra: experiment versus theory. *J. Neurosci.*, *34*, 14589–14605.

Bédard, C., Krüger, H. & Destexhe, A. (2006) Does the $1/f$ frequency scaling of brain signals reflect self-organized critical states? *Phys. Rev. Lett.*, *97*, 118102.

Bracewell, R. (1965) *The Fourier transform and its applications.* New York: McGraw-Hill.

Bremer, F. (1958) Cerebral and cerebellar potentials. *Physiol. Rev.*, *38*, 357–388.

Buzsáki, G. (2006) *Rhythms of the brain.* New York: Oxford University Press.

Buzsáki, G. & Wang, X. J. (2012) Mechanisms of gamma oscillations. *Annu. Rev. Neurosci.*, *35*, 203–225.

Cannon, S. C., Robinson, D. A. & Shamma, S. (1983) A proposed neural network for the integrator of the oculomotor system. *Biol. Cybern.*, *49*, 127–136.

Cebolla, A. M., Petieau, M., Dan, B., Balazs, L., McIntyre, J. & Cheron G (2016) "Cerebellar contribution to visuo-attentional alpha rhythm: insights from weightlessness". *Sci. Rep.*, *6*, 37824.

Chu, Z., Galarreta, M. & Hestrin, S. (2003) Synaptic interactions of late-spiking neocortical neurons in layer 1. *J. Neurosci.*, *23*, 96–102.

Courtemanche, R., Robinson, J. C. & Aponte, D. I. (2013) Linking oscillations in cerebellar circuits. *Front. Neural Circuits*, *7*, 125.

Dehghani, N., Bédard, C., Cash, S. S., Halgren, E. & Destexhe, A. (2010) Comparative power spectral analysis of simultaneous elecroencephalographic and magnetoencephalographic recordings in humans suggests non-resistive extracellular media. *J. Comput. Neurosci.*, *29*, 405–421.

Einevoll, G. T., Kayser, C., Logothetis, N. K. & Panzeri, S. (2013) Modelling and analysis of local field potentials for studying the function of cortical circuits. *Nat. Rev. Neurosci.*, *14*, 770–785.

El Boustani, S., Marre, O., Béhuret, S., Baudot, P., Yger, P., Bal, T., Destexhe, A & Frégnac, Y. (2009) Network-state modulation of power-law frequency-scaling in visual cortical neurons. *PLoS Comput. Biol.*, *5*, e1000519.

Franklin, J. & Bair, W. (1995) The effect of a refractory period on the power spectrum of neuronal discharge. *SIAM J. Appl. Math.*, *55*, 1074–1093.

Freeman, W. J. & Zhai, J. (2009) Simulated power spectral density (PSD) of background electrocorticogram (ECoG). *Cogn. Neurodyn.*, *3*, 97–103.

Fries, P., Womelsdorf, T., Oostenveld, R. & Desimone, R. (2008) The effects of visual stimulation and selective visual attention on rhythmic neuronal synchronization in macaque area V4. *J. Neurosci.*, *28*, 4823–4835.

Gao, R., Peterson, E. J. & Voytek, B. (2017) Inferring synaptic excitation/inhibition balance from field potentials. *NeuroImage*, *158*, 70–78.

Gloor, P. (1985) Neuronal generators and the problem of localization in electroencephalography: application of volume conductor theory to electroencephalography. *J. Clin. Neurophysiol.*, *2*, 327–354.

Gratiy, S. L., Pettersen, K. H., Einevoll, G. T. & Dale, A. M. (2013) Pitfalls in the interpretation of multielectrode data: on the infeasibility of the neuronal current-source monopoles. *J. Neurophysiol.*, *109*, 1681–1682.

Haegens, S., Nácher, V., Luna, R., Romo, R. & Jensen, O. (2011) α-Oscillations in the monkey sensorimotor network influence discrimination performance by rhythmical inhibition of neuronal spiking. *Proc. Natl. Acad. Sci. U. S. A.*, *108*, 19377–19382.

Haegens, S., Barczak, A., Musacchia, G., Lipton, M. L., Mehta, A. D., Lakatos, P. & Schroeder, C. E. (2015) Laminar profile and physiology of the α rhythm in primary visual, auditory, and somatosensory regions of neocortex. *J. Neurosci.*, *35*, 14341–14352.

Haider, B., Schulz, D. P., Häusser, M. & Carandini, M. (2016) Millisecond coupling of local field potentials to synaptic currents in the awake visual cortex. *Neuron*, *90*, 35–42.

Halnes, G., Mäki-Marttunen, T., Keller, D., Pettersen, K. H., Andreassen, O. A. & Einevoll, G. T. (2016) Effect of ionic diffusion on extracellular potentials in neural tissue. *PLoS Comput. Biol.*, *12*, e1005193.

He, B. J. (2014) Scale-free brain activity: past, present, and future. *Trends Cogn. Sci.*, *18*, 480–487.

Hestrin, S. & Galarreta, M. (2005) Electrical synapses define networks of neocortical GABAergic neurons. *Trends Neurosci.*, *28*, 304–309.

Hormuzdi, S. G., Pais, I., LeBeau, F. E., Towers, S. K., Rozov, A., Buhl, E. H., Whittington, M. A. & Monyer, H. (2001) Impaired electrical signaling disrupts gamma frequency oscillations in connexin 36-deficient mice. *Neuron*, *31*, 487–495.

Hughes, S. W., Lörincz, M. L., Blethyn, K., Kékesi, K. A., Juhász, G., Turmaine, M., Parnavelas, J. G. & Crunelli, V. (2011) Thalamic gap junctions control local neuronal synchrony and influence macroscopic oscillation amplitude during EEG alpha rhythms. *Front. Psychol.*, *2*, 193.

Lainscsek, C., Muller, L. E., Sampson, A. L. & Sejnowski, T. J. (2017) Analytical derivation of nonlinear spectral effects and $1/f$ scaling artifact in signal processing of real-world data. *Neural Comput.*, *29*, 2004–2020.

Lee, S. C., Patrick, S. L., Richardson, K. A. & Connors, B. W. (2014) Two functionally distinct networks of gap junction-coupled inhibitory neurons in the thalamic reticular nucleus. *J. Neurosci.*, *34*, 13170–13182.

Łęski, S., Lindén, H., Tetzlaff, T., Pettersen, K. H. & Einevoll, G. T. (2013) Frequency dependence of signal power and spatial reach of the local field potential. *PLoS Comput. Biol.*, *9*, e1003137.

Lindén, H., Pettersen, K. H. & Einevoll, G. T. (2010) Intrinsic dendritic filtering gives low-pass power spectra of local field potentials. *J. Comput. Neurosci.*, *29*, 423–444.

Lombardi, F., Herrmann, H. J. & de Arcangelis L. (2017) Balance of excitation and inhibition determines $1/f$ power spectrum in neuronal networks. *Chaos*, *27*, 047402.

Lorente de Nó, R. (1947) Action potential of the motoneurons of the hypoglossus nucleus. *J. Cell. Comp. Physiol.*, *29*, 207–287.

Lozano-Soldevilla, D., ter Huurne, N., Cools, R. & Jensen, O. (2014) GABAergic modulation of visual gamma and alpha oscillations and its consequences for working memory performance. *Curr. Biol.*, *24*, 2878–2887.

Maex, R. & De Schutter, E. (2003) Resonant synchronization in heterogeneous networks of inhibitory neurons. *J. Neurosci.*, *23*, 10503–10514.

Maex, R. & Gutkin, B. (2017) Temporal integration and $1/f$ power scaling in a circuit model of cerebellar interneurons. *J. Neurophysiol.*, *118*, 471–485.

Mazzoni, A., Panzeri, S., Logothetis, N. K. & Brunel, N. (2008) Encoding of naturalistic stimuli by local field potential spectra in networks of excitatory and inhibitory neurons. *PLoS Comput. Biol.*, *4*, e1000239.

Mazzoni, A., Lindén, H., Cuntz, H., Lansner, A., Panzeri, S., & Einevoll, G. T. (2015) Computing the local field potential (LFP) from integrate-and-fire network models. *PLoS Comput. Biol.*, *11*, e1004584.

Middleton, S. J., Racca, C., Cunningham, M. O., Traub, R. D., Monyer, H., Knöpfel, T., Schofield, I. S., Jenkins, A. & Whittington, M. A. (2008) High-frequency network oscillations in cerebellar cortex. *Neuron*, *58*, 763–774.

Neske, G. T. (2016) The slow oscillation in cortical and thalamic networks: mechanisms and functions. *Front. Neural Circuits*, *9*, 88.

Neske, G. T. & Connors, B. W. (2016) Synchronized gamma-frequency inhibition in neocortex depends on excitatory-inhibitory interactions but not electrical synapses. *J. Neurophysiol.*, *116*, 351–368.

Ness, T. V., Remme, M. W. & Einevoll, G. T. (2016) Active subthreshold dendritic conductances shape the local field potential. *J. Physiol.*, *594*, 3809–3825.

Nicholson, C. & Freeman, J. A. (1975) Theory of current source-density analysis and determination of conductivity tensor for anuran cerebellum. *J. Neurophysiol.*, *38*, 356–368.

Niedermeyer, E. (2004) The electrocerebellogram. *Clin. EEG Neurosci.*, *35*, 112–115.

Novikov, E., Novikov, A., Shannahoff-Khalsa, D., Schwartz, B. & Wright, J. (1997) Scale-similar activity in the brain. *Phys. Rev. E*, *56*, R2387.

Nunez, P. L. (1981) *Electric fields of the brain: The neurophysics of EEG* (1st ed.). New York: Oxford University Press.

Pettersen, K. H., Lindén, H., Tetzlaff, T. & Einevoll, G. T. (2014) Power laws from linear neuronal cable theory: power spectral densities of the soma potential, soma membrane current and single-neuron contribution to the EEG. *PLoS Comput. Biol.*, *10*, e1003928.

Plonsey, R. (1964) Volume conductor fields of action currents. *Biophys. J.*, *4*, 317–328.

Podvalny, E., Noy, N., Harel, M., Bickel, S., Chechik, G., Schroeder, C. E., Mehta, A. D., Tsodyks, M. & Malach, R. (2015) A unifying principle underlying the extracellular field potential spectral responses in the human cortex. *J. Neurophysiol.*, *114*, 505–519.

Press, W. H., Teukolsky, S. A., Vetterling, W. & Flannery, B. P. (2007) *Numerical recipes : The art of scientific computing* (3rd ed.). New York: Cambridge University Press.

Rall, W. & Shepherd, G. M. (1968) Theoretical reconstruction of field potentials and dendrodendritic synaptic interactions in olfactory bulb. *J. Neurophysiol.*, *31*, 884–915.

Reimann, M. W., Anastassiou, C. A., Perin, R., Hill, S. L., Markram, H. & Koch, C. (2013) A biophysically detailed model of neocortical local field potentials predicts the critical role of active membrane currents. *Neuron*, *79*, 375–390.

Rosen, M. J. (1972) A theoretical neural integrator. *IEEE Trans. Biomed. Eng.*, *19*, 362–367.

Schwalger, T., Deger, M. & Gerstner, W. (2017) Towards a theory of cortical columns: From spiking neurons to interacting neural populations of finite size. *PLoS Comput. Biol.*, *13*, e1005507.

Schroeder, M. R. (1991) *Fractals, chaos, power laws: minutes from an infinite paradise.* New York: W. H. Freeman and Company.

Stumpf, M. P. & Porter M. A. (2012) Critical truths about power laws. *Science*, *335*, 665–666.

Thomas, C. W. (2015) Coherence function in noisy linear system. *International Journal of Biomedical Science and Engineering*, *3*, 25–33.

Tremblay, R., Lee, S. & Rudy, B. (2016) GABAergic interneurons in the neocortex: from cellular properties to circuits. *Neuron*, *91*, 260–292.

Van Dijck, G., Seidl, K., Paul, O., Ruther, P., Van Hulle, M. M. & Maex, R. (2012) Enhancing the yield of high-density electrode arrays through automated electrode selection. *Int. J. Neural Syst.*, *22*, 1–19.

van Kerkoerle, T., Self, M. W., Dagnino, B., Gardel-Mathis, M. A., Poort, J., van der Togt, C., Roelfsema, P. R. (2014) Alpha and gamma oscillations characterize feedback and feedforward processing in monkey visual cortex. *Proc. Natl. Acad. Sci. U. S. A.*, *111*, 14332–14341.

Wang, X. J. & Buzsáki, G. (1996) Gamma oscillation by synaptic inhibition in a hippocampal interneuronal network model. *J. Neurosci.*, *16*, 6402–6413.

Wilson, M. A. & Bower, J. M. (1989) The simulation of large-scale neural networks, in: *Methods in neuronal modeling* (C. Koch and I. Segev, eds.). Cambridge (MA): MIT Press, pp. 291–333.